Visualization of Sub-atomic Movements in Nanostructures

Tongjun Liu[*], *Jun-Yu Ou*[*, ‡], *Eric Plum*[*], *Kevin F. MacDonald*[*, ‡], *Nikolay I. Zheludev*[*†]

* Optoelectronics Research Centre and Centre for Photonic Metamaterials, University of Southampton, Highfield, Southampton, SO17 1BJ, UK

† Centre for Disruptive Photonic Technologies, School of Physical and Mathematical Sciences and The Photonics Institute, Nanyang Technological University, Singapore, 637378, Singapore

‡ E-mail: Bruce.Ou@soton.ac.uk; kfm@orc.soton.ac.uk

ABSTRACT: Electron microscopy, scanning probe and optical super-resolution imaging techniques with nanometric resolution are now routinely available but cannot capture the characteristically fast (MHz-GHz frequency) movements of micro/nano-objects. Meanwhile, optical interferometric techniques can detect high frequency picometric displacements but only with diffraction limited lateral resolution. Here, we introduce a motion visualization technique, based upon spectrally resolved detection of secondary electron emission from moving objects, that combines picometric displacement sensitivity with the nanometric spatial (positional/imaging) resolution of electron microscopy. The sensitivity of the technique is quantitatively validated against the thermodynamically defined amplitude of a nano-cantilever's Brownian motion. It is further demonstrated in visualizing externally driven modes of cantilever, nanomechanical photonic metamaterial and MEMS device structures. With a noise floor reaching ~1 pm/Hz$^{1/2}$, it can provide for the study of oscillatory movements with sub-atomic amplitudes, presenting new opportunities for the interrogation of motion in functional structures across the materials, bio- and nano-sciences.

KEYWORDS: *nanomechanics, thermal motion, electron microscopy, metrology*

Introduction

Nanoscale motion is of growing technological importance and scientific interest, in contexts including: micro- and nano-electro-mechanical systems (MEMS and NEMS)[1, 2], such as the accelerometers found in every smartphone and the optical fiber switches employed in optical communications/data networks[3]; advanced materials, from nanoparticles, nanowires and 2D nanomaterials (e.g. graphene, transition metal dichalcogenides) to mechanically-reconfigurable photonic metamaterials with optical properties that can be switched/tuned via nanometric

distortion or displacement of constituent meta-molecules[4]; and in fundamental studies of dynamics, including cooperative and self-organizational effects, in nano- and (bio)molecular systems governed by thermal (Brownian) motion, Van der Waals and Casimir forces, and quantum phenomena[5-13 14, 15].

However, there are no routinely available techniques for mapping fast, complex motion at the nano- to picoscale with high temporal and spatial resolution. Transmission and scanning electron microscopes, scanning probe techniques (STM, AFM, etc.) and optical super-resolution microscopies ('PALM'/'STED'/'STORM'[16-19], and recently introduced methodologies employing superoscillatory and topologically structured light fields[20-22] provide nanometric or better spatial resolution in 'static' imaging. But limited measurement/frame rates mean that they cannot generally resolve high-frequency motion at such scales. 'Time-resolved' or 'ultrafast' electron microscopes[23, 24] are highly-specialized instruments employing short-pulse (typically fs laser-driven) electron sources and streak camera or time-correlated photon counting detectors to interrogate stimulated, short-timescale (e.g. carrier, lattice and bonding) dynamics in materials in pump-probe and stroboscopic regimes. Laser-based interferometric and cavity spectroscopic techniques[25, 26] can provide MHz frequency picometric sensitivity to changes in optical path length (i.e. in the direction of light propagation) but, for imaging purposes in the transverse direction, they are diffraction-limited with spatial resolution of a few hundred nanometers at best.

Here, we introduce a technique for hyperspectral motion visualization (HMV), which that combines sensitivity to movement of sub-atomic amplitude with the nanometric spatial resolution of scanning electron microscopy (SEM). Quantitative, directionally-resolved measurements and mapping of displacement amplitude and relative phase, providing for highly localized interrogation of mechanical resonance characteristics (Eigenfrequencies, quality factors) of target structures and visualization of their mechanical modes.

The Hyperspectral Motion Visualization (HMV-SEM) concept

The functional principle behind the motion visualization technique is illustrated in Fig. 1. Conventional SEM images are formed by raster scanning a focused electron beam over an object and detecting, at each point, the integrated secondary or backscattered electron current. Any fast-moving components of the object (the wings and antennae of the bee in Fig. 1a) will suffer 'motion-blur' because their displacement cannot be tracked on timescales shorter than the frame rate. However, by instead recording the time dependence of the secondary electron (SE) current at each point one can detect and spatially map fast movements of the object. One may then record either full raster-scanned images with SE detection locked at a chosen frequency, or construct a complete hyperspectral image by computing the Fourier spectrum of motion at each point. These 'images' will show spatially resolved, quantitative detail of displacement amplitude and phase at a chosen frequency or across a range of frequencies. For simple objects, much useful information can be obtained from images recorded at just a few selected frequencies, as will be demonstrated in what follows.

Figure 1(b-d) details the mechanism by which the SE signal generated by an incident electron beam transduces oscillatory displacements[27, 28]. While the target object (notionally one of the bee's antennae in Fig. 1a) is stationary, the SE current $I_{SE}(\boldsymbol{r})$ generated as an incident electron beam is

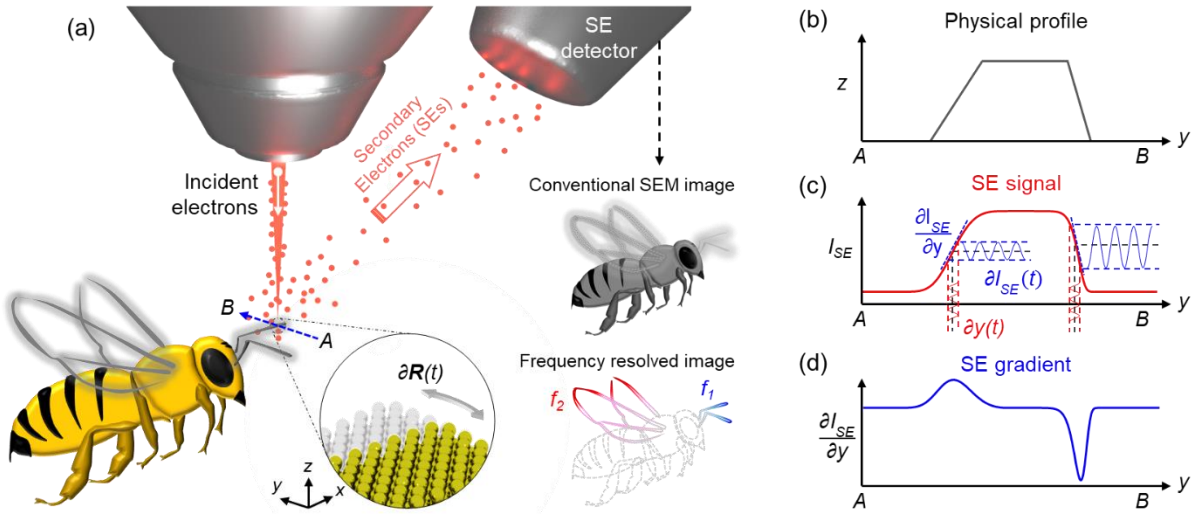

Figure 1. Hyperspectral Motion Visualization (HMV-SEM) concept. (a) Conventional (static) secondary electron (SE) images obtained in a scanning electron microscope are based upon the time-averaged SE signal at each point, whereby moving parts suffer 'motion blur'. HMV-SEM maps based upon the detection of selected frequency components in the SE signal will show only those parts which oscillate at that frequency, revealing the amplitude and direction of movement at each point. [Bee images are derived from bee-wingpath-animation-4 © Arizona Board of Regents / ASU Ask A Biologist under CC BY-SA 3.0 license - colors changed and/or blur selectively added.] (b-d) An incident electron beam scanned over an object [notionally here, one of the bee's antennae, along the line AB in (a)] generates a scattered secondary electron signal with an amplitude profile (c) related to the physical profile of the object (b) and the spot size and intensity profile of the incident electron beam. Where the gradient (d) of this profile is non-zero, displacements of the object ∂y translate to changes in SE signal ∂I_{SE}, as illustrated inset to (c).

scanned along the line *AB* (where $\boldsymbol{r}$ is coordinate in the image plane) will change in magnitude from and return to zero on either side (where the incident beam entirely misses the object) at a rate dependent upon the sharpness of the physical edges and the intensity profile of the electron beam. At these edges, small time-dependent displacements $\partial\boldsymbol{R}(t)$ of the object will translate to changes in the SE signal:

$$\frac{\partial I_{SE}(\boldsymbol{r},\boldsymbol{R}(t))}{\partial t} = \frac{\partial I_{SE}(\boldsymbol{r},\boldsymbol{R}(t))}{\partial \boldsymbol{R}} \cdot \frac{\partial \boldsymbol{R}}{\partial t} = -\nabla I_{SE}(\boldsymbol{r}) \cdot \boldsymbol{v}(t) \qquad (1)$$

where $\boldsymbol{v}$ is the object's movement velocity vector at the measurement point. Integrated over time:

$$I_{SE}(\boldsymbol{r},t) = -\nabla I_{SE}(\boldsymbol{r}) \cdot \boldsymbol{R}(t) + C \qquad (2)$$

Thus, at each point on the oscillating target, the magnitude of the time-dependent SE signal will be equal to the scalar product of two vectors: the gradient of the static SEM image parallel to the motion direction at that point $\nabla I_{SE}(\boldsymbol{r})$ and the displacement $\boldsymbol{R}(t)$. As such, motion in any direction with a non-zero projection to the image plane can be detected at any point where the corresponding

SE gradient is non-zero. In the Fig. 1 schematic, for example, if the image plane is inclined at an angle θ to the y axis, both horizontal $\partial y(t)$ and vertical $\partial z(t)$ displacements of the object (in and out of the xy sample plane) can be detected on the basis of a SE signal gradient parallel to y.

The noise equivalent displacement (NED) level in such measurements – the magnitude of oscillatory displacement detectable with unitary signal-to-noise ratio with an integration time of one second - is determined largely by the Poisson statistics of electrons incident on the SE detector. It is inversely proportional to the SE current gradient ∇I_{SE} (see Supporting Information). For a typical SEM, this noise-limited minimum detectable displacement amplitude can be as small as ~1 pm in phase-locked measurements even while the incident beam diameter (which constrains static imaging resolution) is ≥1 nm. The ability to detect motion at this scale presents remarkable opportunities for imaging the movement of nanostructures, bearing in mind that by comparison the lattice constants of solids are typically in the 300-700 pm range and the radii of isolated neutral atoms lie between 30 and 300 pm.

Hyperspectral Motion Visualization

To elucidate and quantitatively validate performance of HMV-SEM we employ rectangular cantilevers, i.e. the common actors and structural components of many nanomechanical devices and systems – objects with well-understood, analytically described modes of oscillation.

Calibration of measurement sensitivity against thermal motion

The random thermal motion of small objects at non-zero temperatures is perhaps most familiar in the microscopic random walk of free particles in liquids, known as Brownian motion. But thermal motion of picometric amplitude is also present in anchored micro/nano objects, such as cantilevers and doubly-clamped beams, and is most profound at their natural mechanical resonant frequencies. Such motion provides an ideal calibration reference for the sensitivity of the HMV-SEM technique as its amplitude is thermodynamically related to physical parameters of the object: which is to say that a direct quantitative comparison can be made between experiment and energy equipartition theorem[29, 30].

To demonstrate, we detect the thermal motion of a 22 μm long cantilever (Fig. 2a) manufactured by focused ion beam milling from a 50 nm thick silicon nitride membrane (a flexible substrate) coated by thermal evaporation with 50 nm of gold (for strong secondary electron signal contrast). With the incident electron beam fixed at a point on one of the cantilever's long edges near to the tip, as indicated in Fig. 2a, we record the time dependence of the secondary electron signal in the frequency domain and calculate its amplitude spectral density (ASD, Fig. 2c). In all measurements reported here we employ an incident electron energy of 5 keV and a beam current of 86 pA, whereby the effects of electron beam-induced heating and momentum transfer to the cantilever are negligible (see Supporting Information). The measured secondary electron signal ASD at a given point is directly related to cantilever displacement ASD (right-hand axis in Fig. 2c) via the SE signal gradient (Fig. 2b) at that point, with account taken for the oblique incidence of the electron beam. We observe peaks in the frequency spectrum at three of cantilever's natural oscillation frequencies: specifically, the fundamental out-of-plane mode at 117.6 kHz, fundamental in-plane mode at 528.0 kHz and second-order out-of-plane mode at 739.0 kHz (attribution of modes being confirmed by computational modelling – see Supporting Information).

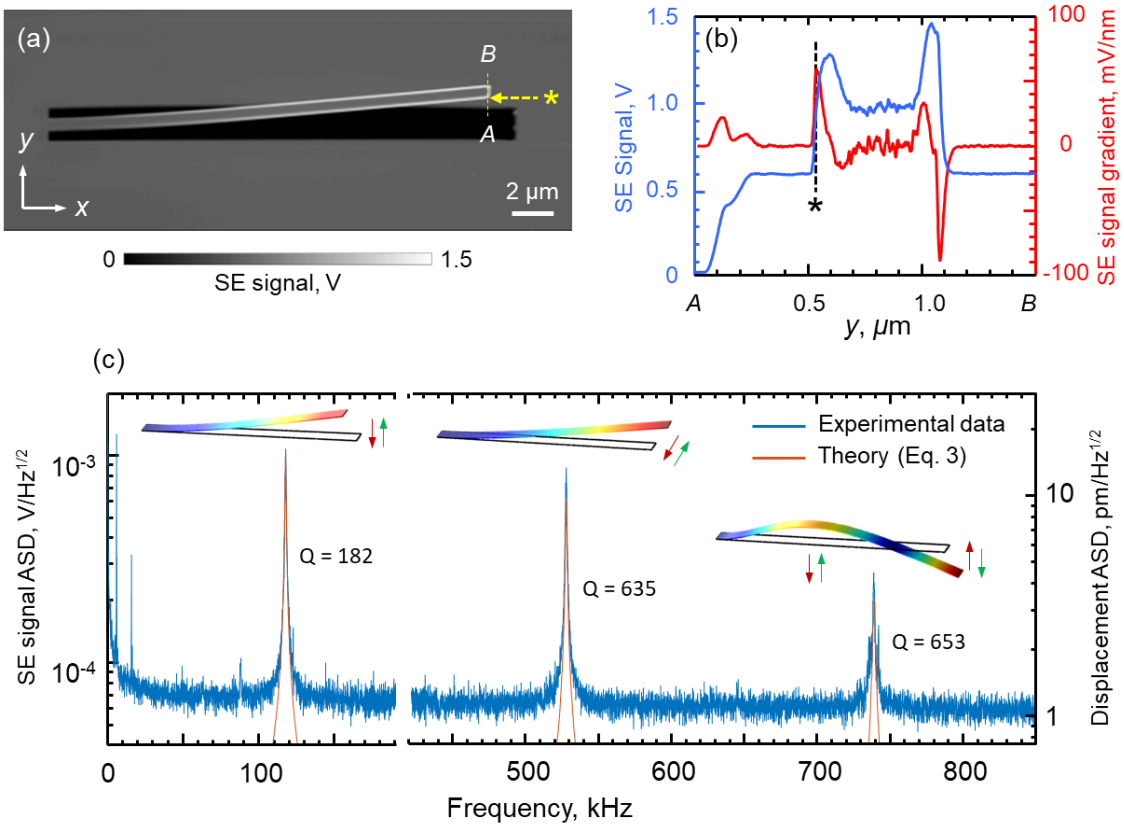

Figure 2. Sensing thermal motion of a cantilever. (a) Static secondary electron image of a gold-coated silicon nitride cantilever [100 nm thick, 500 nm wide, 22 μm long], viewed at an oblique angle $\theta = 15°$ to the membrane plane. (b) Profile along the line *AB* of secondary electron DC signal and the gradient thereof. (c) Amplitude spectral density (ASD) of secondary electron signal measured at the point *, showing peaks associated with out-of- and in-plane oscillatory modes [as denoted by the inset schematics]. The right-hand axis shows a calibrated scale of displacement ASD. Overlaid red lines are analytical displacement ASD curves given by Eq. (3), using experimentally measured values of f_0 and Q for each mode, and assuming $m_{\text{eff}} = 0.25m$.

According to the Wiener–Khinchin theorem[29, 30], the thermomechanical displacement power spectral density (PSD = ASD^2) of an oscillator is

$$S(f) = \frac{k_B T f_0}{2\pi^3 m_{\text{eff}} Q[(f_0^2 - f^2)^2 + (f f_0/Q)^2]} \qquad (3)$$

where k_B is the Boltzmann constant, T is temperature and, for each mode, m_{eff}, f_0 and Q are respectively the effective mass (see Supporting Information), natural frequency and quality factor. From experiment – the mapping of Eq. (3) onto the peaks in Fig. 2c using measured values of f_0 and Q at room temperature ($T = 300$ K), with m_{eff} determined by best fit – root mean square (RMS) thermal motion amplitudes x_{th} can be evaluated as the square root of an integral of PSD over frequency:

$$x_{th} = \sqrt{\int_0^\infty S(f)df} \qquad (4)$$

These calculations yield amplitudes of 1.60 nm for the out-of-plane mode at 117.6 kHz; 0.53 nm for the in-plane mode at 528.0 kHz; and 0.27 nm for the second-order out-of-plane mode at 739.0 kHz. These compare very well with analytical values of 1.57, 0.35 and 0.25 nm respectively, from thermal equipartition for an ideal rectangular cantilever, whereby $x_{th} = \sqrt{k_B T / m_{\text{eff}}(2\pi f_0)^2}$ and m_{eff} has a fixed value of $0.25m$ for all modes (m being the real mass – see Supporting Information). The accuracy of the correlation between theory and experiment is illustrated in Fig. 2c by the overlaid analytical curves, which are calculated according to Eq. (3) with $m_{\text{eff}} = 0.25$. Likewise, the ~1 pm/Hz$^{1/2}$ background signal level seen in Fig 2c corresponds very well with the expected noise equivalent displacement floor (see above and Supporting Information).

Full-width half-maximum peak widths Δf are a measure of oscillator damping: $\Delta f = \gamma / 2\pi m_{\text{eff}}$, where γ is the (material, ambient pressure, and mode-dependent) dissipation factor or effective viscosity[31, 32]. With the effective mass of a cantilever being, again, not mode-dependent (see Supporting Information) peak width Δf is straightforwardly proportional to, and resonance quality $Q = f_0/\Delta f$ inversely proportional to, γ.

Driven Motion

HMV-SEM can also be applied to mapping externally-driven movements of nanostructures. By raster scanning the injection point over a target and synchronously detecting the SE signal at the driving frequency (using a lock-in amplifier), a spatially resolved map of driven oscillation amplitude and phase can be constructed, giving a comprehensive picture of the sample's mechanical response at the selected frequency. By then changing the driving frequency and repeating the raster scan, a hyperspectral image of sample movements can be assembled.

We demonstrate this modality by visualizing the oscillatory motion of cantilevers driven by a piezoelectric transducer (with an oscillatory amplitude of ≤1 nm). Figures 3a-c show images of the above (Fig. 2) cantilever in terms of, respectively, the DC component (c.f. static SE image) and the amplitude and phase of the time-dependent component of the SE signal at 739.0 kHz - the frequency of its second-order out-of-plane bending mode. These illustrate how the technique reveals movement at the high SE contrast edges of a structure: no signal is detected where the SE gradient is zero (along the central area of the cantilever surface). In this case, each bright edge of the cantilever in Fig. 3a appears as a pair of lines in Fig. 3b with opposing phase relative to the piezo actuator (Fig. 3c), corresponding to closely-spaced points of positive and negative SE gradient encountered as the incident electron beam is scanned across the edge. An out-of-plane displacement amplitude map (Fig. 3d) is obtained by dividing the time-dependent SE signal amplitude at each point of Fig. 3b by the corresponding signal gradient derived from Fig. 3a (see Supporting Information), taking account of the oblique viewing angle. Combining this with the signal phase and plotting all pixels as a histogram of absolute displacement against x coordinate, reveals the displacement mode shape, as shown in Fig. 3e. In this example, the cantilever tip oscillates with amplitude of ~25 nm.

To illustrate hyperspectral motion visualization, we employ a set of three cantilevers with different lengths (17, 22 and 27 μm) cut from a single membrane (Fig. 4). Having first identified their individual natural frequencies from thermal motion spectra (as per Fig. 2 above), we then drive

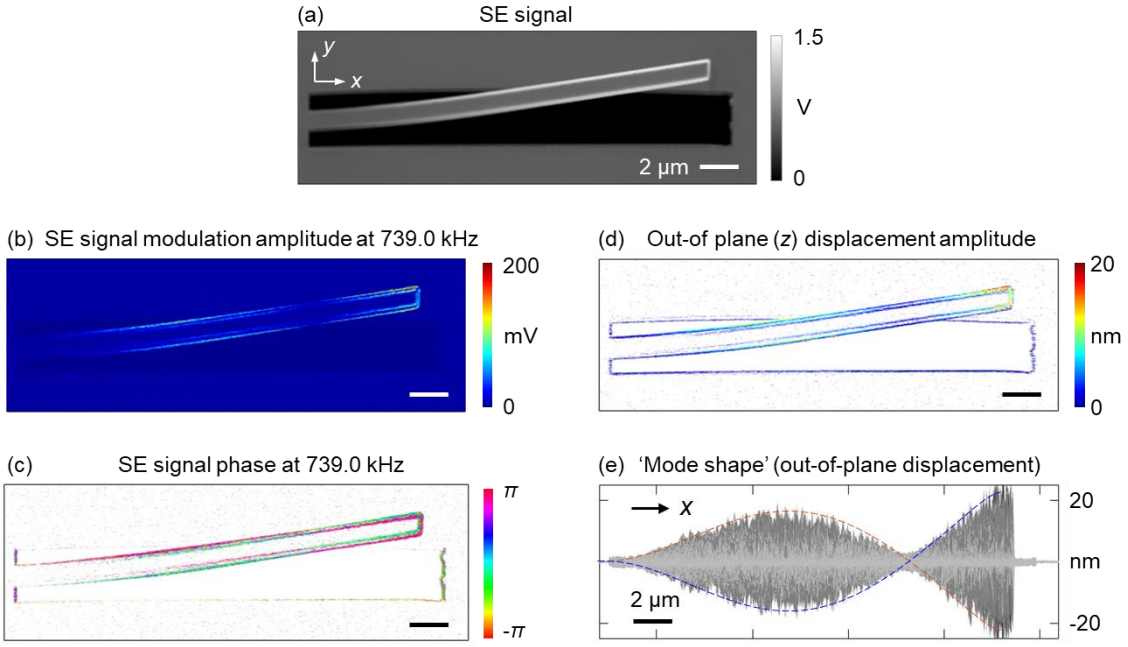

Figure 3. Visualization of driven cantilever motion. (a-c) DC component (a) and synchronously recorded amplitude and phase (b and c respectively) of the time-dependent component of the secondary electron signal recorded while the structure is mechanically driven at the cantilever's 739.0 kHz 2nd-order out-of-plane resonant frequency by a piezo-actuator. (d) Calibrated out-of-plane [*z*-direction] displacement amplitude maps of the cantilever. (e) *x*-*z* plane projection of absolute displacement with the corresponding numerically simulated mode profile overlaid as a pair of dashed lines. Note that the vertical image-plane scale [panels a-d] has been enlarged for clarity: the 2 µm scale bar applies only to the *x* direction. Also for clarity in (d), no data is presented at points where the SE gradient falls below a noise threshold, i.e. such that displacement cannot be quantified. The same [white] pixels are then also excluded from (c).

the structure and spatially map the movement of the whole sample at each frequency in turn (Fig. 4a). The selective, resonant excitation of one cantilever at a time in either its fundamental or second-order out-of-plane bending modes is clearly observed, with the expected mode shapes being well defined in corresponding *x*-*z* projections of displacement (Fig. 4b).

Visualization of movement in devices with multiple degrees of freedom

The examples presented above introduce the HMV-SEM technique by way of its use to study thermal and driven motion of isolated cantilevers. However, its full potential lies in application to understanding behaviors and functionalities in more complex structures and devices with multiple degrees of freedom – the 'nano-machines' of Feynman's famous 1959 lecture "There's Plenty of Room at the Bottom"[33]. Micro- and nano-electromechanical system (M/NEMS)[2] and nano-mechanical metamaterials[34] have since become practical implementations of this idea.

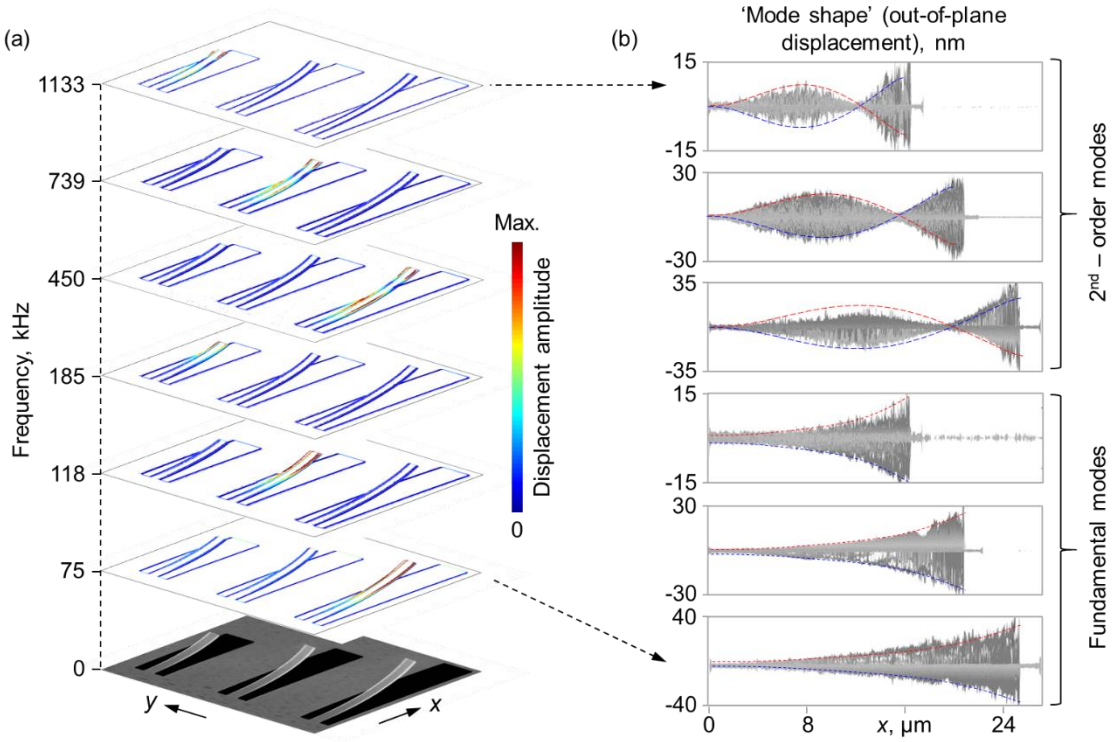

Figure 4. Hyperspectral visualization of driven cantilever motion. (a) Out-of-plane [*z*-direction] displacement amplitude maps of a set of three cantilevers of different length, shown in the zero-frequency [static secondary electron] image, recorded while the structure is mechanically driven at a selection of frequencies [as labelled] by a piezo-actuator. (b) Corresponding *x*-*z* plane projections of absolute displacement overlaid with numerically simulated mode profiles (dashed lines).

Figure 5a shows an SEM image of a plasmonic nano-opto-mechanical metamaterial comprising an array of gold nano-brick trimers supported on alternately wide (325 nm) and narrow (165 nm) 28 µm long, 50 nm thick silicon nitride beams. This metamaterial presents an exceptionally large optical nonlinearity underpinned by the mutual nanoscale displacement of neighboring beams, driven by interactions between dipole moments induced in the plasmonic nano-bricks by a control (pump) light beam[35]. Ideally, a modulated pump beam will induce synchronous resonant (i.e. large amplitude) oscillation of all wide or narrow structural beams, thereby maximizing the induced change in transmission or reflection of a probe beam. As such, the nonlinear optical response of the metamaterial is dependent on the mechanical properties of the structure, specifically the natural frequencies and quality factors of the beams. All beams of the same type should preferably be mechanically identical to exclude inhomogeneous broadening of the nonlinearity. HMV-SEM is ideally suited to the task of interrogating the properties of individual structural beams.

The thermal motion spectra in Fig. 5b reveal variations in the mechanical properties of a set of nominally identical beams: the fifteen narrow beams of the metamaterial shown have fundamental in-plane resonant frequencies of 1.44 MHz ±2%, mean square displacement amplitudes of 209 pm

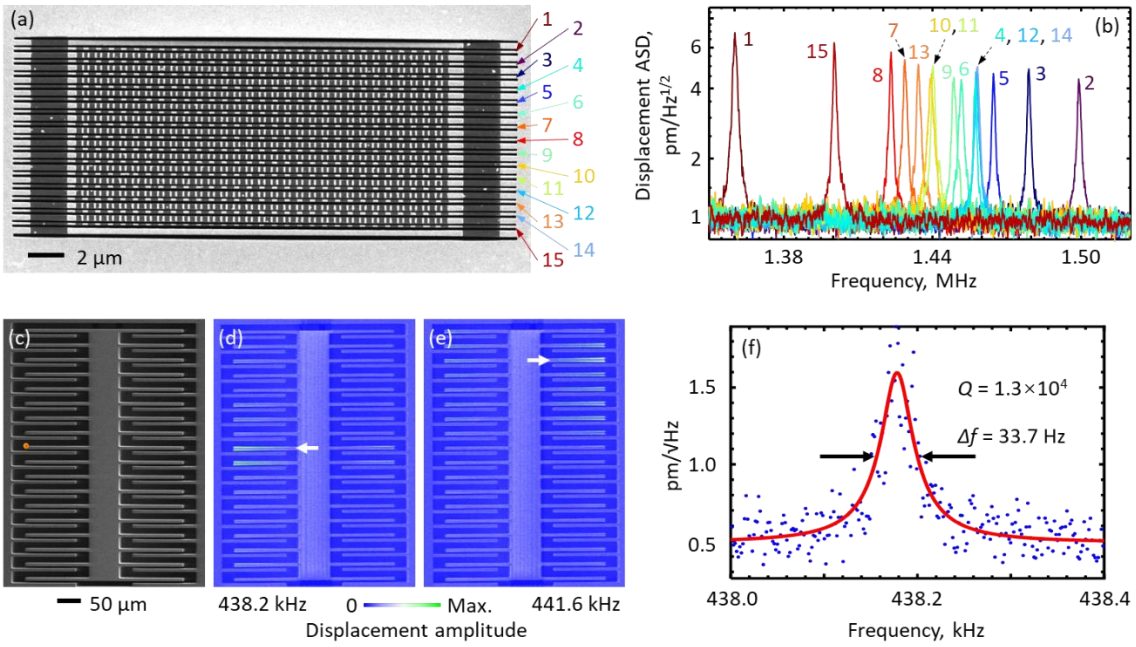

Figure 5. Mapping thermal and driven motion in photonic metamaterials and MEMS devices. (a) SEM image of an optomechanical metamaterial fabricated on a silicon-nitride nanomembrane (b) In-plane thermal motion displacement spectra measured at the centers of the fifteen narrow beams [as numbered in (a)]. (c) SEM image of a capacitive Si comb within a MEMS accelerometer. (d, e) Corresponding displacement amplitude maps for piezo actuator-driven in-plane motion at 438.2 and 441.6 kHz – the fundamental resonant frequencies of selected comb cantilever 'fingers' [marked by white arrows]. (f) Representative thermal motion spectrum measured at the tip of the comb cantilever finger marked with a red dot in (c).

±6% and quality factors of 1400 ±33%. With the peripheral beams numbered 1, 2 and 15 excluded, these distributions narrow to ±1% in resonant frequency, ±4% in displacement amplitude and ±5% in Q. From static SEM imaging, those three beams are subject to noticeable equilibrium out-of-plane deformation, but variations in mechanical properties among the majority cannot be anticipated – they are seen to have a high level of geometric uniformity, constrained only by the nanometric fabrication tolerances of the FIB milling technique. However, variations in their mechanical parameters are related not only to dimensional discrepancies or fabrication imperfections, but also to variations in tension (in the same way that tension determines the pitch of a violin string) derived from non-uniform stress intrinsic to the silicon nitride membrane substrate. The ability to quantify the mechanical response of the individual structural elements of a metamaterial provides valuable insight to device performance and provides for the possibility of in-situ correction during fabrication (i.e. within a dual-beam FIB/SEM system), thus enabling the fabrication of high-performance devices.

Figure 5c shows an SEM image of a silicon capacitive comb sensing element within a commercial MEMS accelerometer developed for automotive air-bag deployment systems. Acceleration in the sensing direction induces an inertial force on the mass attached to the movable part of the comb, resulting in a change in distance between the 'fingers' of the fixed and movable parts of the comb.

From the associated change in capacitance, acceleration can be quantified. Device behaviors including sensitivity and false alarm response depend strongly upon the mechanical characteristics of the comb fingers, which are in effect micromechanical cantilevers, and controlled artificial displacements of the inertial mass may be applied to the detection of defective combs. Using the HMV-SEM technique (Figs. 5d-f), we find that the nominally identical fingers of the present comb indeed have closely spaced fundamental resonant frequencies - varying by only ±0.4% about a mean value of 440 Hz, and resonance Q-factors of order 1.4×10^4 that vary by as much as ±8%. The fingers manifest in-plane thermal motion tip displacements of ~25 pm (as compared to a separation between adjacent fingers of ~5μm).

Conclusion

In summary, we have developed a methodology for quantitative, directionally-resolved measurements of high-frequency oscillatory movements with picometric (sub-atomic) amplitudes and the hyperspectral visualization of the movement with nanometric spatial resolution. HMV-SEMcan be deployed on conventional scanning electron microscopes to interrogate thermal (Brownian), self-propelled and externally-driven motion (including in short-timescale and nonlinear regimes) at the pico- to nanoscale. It is shown to provide for: highly localized measurement of oscillators' resonant frequencies and quality factors; measurement of thermal motion amplitudes down to a noise-equivalent displacement level of 1 $pm/Hz^{1/2}$; and frequency- and directionally-resolved mapping of oscillatory motion 'mode shapes' with spatial (SEM imaging) resolution far beyond the diffraction limit applicable to optical vibrometry techniques. The technique is demonstrated here on the basis of secondary electron detection but may equally be applied to other modes of SEM signal generation (e.g. backscattered electrons, sample current, cathodoluminescence). It is subject to the same constraints on target conductivity as any conventional imaging modes and, as for such modes, 'environmental' (low vacuum) systems can facilitate direct application to less conductive (e.g. dielectric, bio) materials, but chamber pressure will affect the mechanical properties of nano/microstructures through atmospheric damping. The methodology can be applied to a wide variety of manmade and naturally occurring nanomaterials, structures, and devices for highly-localized evaluation of material parameters (e.g. Young's modulus), mass sensing, micro/nano-device manufacturing process control and optimization, non-destructive testing, and the study of forces and fields at the (sub)nanometer scale. As a frequency-resolved methodology it complements established (ultrafast) time-resolved electron microscopy techniques: the latter being ideally suited to the study of transient phenomena in time-series measurements with picosecond resolution; the former to oscillatory motion with picometric displacement amplitude sensitivity; both with nanometric spatial (imaging) resolution.

ASSOCIATED CONTENT

Supporting Information. Contains further detail on: Noise Equivalent Displacement (NED); Electron beam-induced heating; Electron-to-cantilever momentum transfer; Cantilever resonance frequencies; Effective mass; and Displacement calibration.

Data availability Following a period of embargo, the data from this paper will be available from the University of Southampton ePrints research repository: https://doi.org/10.5258/SOTON/D1916.

AUTHOR INFORMATION

Corresponding Authors

Jun-Yu Ou − orcid.org/0000-0001-8028-6130; Email: Bruce.Ou@soton.ac.uk

Kevin F. MacDonald − orcid.org/0000-0002-3877-2976; Email: kfm@orc.soton.ac.uk

Authors

Tongjun Liu − orcid.org/0000-0003-4931-1734

Eric Plum − orcid.org/0000-0002-1552-1840

Nikolay I. Zheludev − orcid.org/0000-0002-1013-6636

Author Contributions

JYO conceived the idea for the experiment. JYO and TL configured the SEM instrumentation. TL manufactured cantilever and metamaterial samples and carried out the measurements. All authors discussed the results, analyzed the data, and contributed to writing the paper. KFM and NIZ supervised the work.

Notes

The authors declare no competing financial interests.

ACKNOWLEDGMENTS

This work is supported by the UK Engineering and Physical Sciences Research Council (grants EP/M009122/1 and EP/T02643X/1), the Singapore Ministry of Education (NIZ - grant MOE2016-T3-1-006) and the China Scholarship Council (TL – grant 201806160012). The authors would like to thank Dr. Innoas Zeimpekis for providing the MEMS accelerometer for characterization.

REFERENCES

1. Ekinci, K.; Roukes, M. *Rev. Sci. Instrum.* **2005,** 76, (6), 061101.
2. Feng, P. X.-L.; Young, D. J.; Zorman, C. A., MEMS/NEMS devices and applications. In *Springer Handbook of Nanotechnology*, Springer: 2017; pp 395-429.
3. Wu, M. C.; Solgaard, O.; Ford, J. E. *J. Lightwave Technol.* **2006,** 24, (12), 4433-4454.
4. Zheludev, N. I.; Plum, E. *Nat. Nanotech.* **2016,** 11, 16-22.
5. Roos, N. *Am. J. Phys.* **2014,** 82, (12), 1161-1166.
6. Li, T.; Kheifets, S.; Medellin, D.; Raizen, M. G. *Science* **2010,** 328, (5986), 1673-1675.
7. Ye, F.; Lee, J.; Feng, P. X.-L. *Nanoscale* **2017,** 9, (46), 18208-18215.
8. Geim, A. K.; Grigorieva, I. V. *Nature* **2013,** 499, (7459), 419-425.

9. Woods, L.; Dalvit, D. A. R.; Tkatchenko, A.; Rodriguez-Lopez, P.; Rodriguez, A. W.; Podgornik, R. *Rev. Mod. Phys.* **2016,** 88, (4), 045003.
10. Tang, L.; Wang, M.; Ng, C.; Nikolic, M.; Chan, C. T.; Rodriguez, A. W.; Chan, H. B. *Nat. Photon.* **2017,** 11, (2), 97.
11. Rodriguez, A. W.; Capasso, F.; Johnson, S. G. *Nat. Photon.* **2011,** 5, 211-221.
12. Bernheim-Groswasser, A.; Gov, N. S.; Safran, S. A.; Tzlil, S. *Adv. Mater.* **2018,** 30, (41), 1707028.
13. Oberhauser, A. F., *Single-molecule Studies of Proteins*. Springer: 2012.
14. Lapolla, A.; Godec, A. *Phys. Rev. Lett.* **2020,** 125, (11), 110602.
15. Khosla, K. E.; Vanner, M. R.; Ares, N.; Laird, E. A. *Phys. Rev. X* **2018,** 8, (2), 021052.
16. Betzig, E.; Patterson, G. H.; Sougrat, R.; Lindwasser, O. W.; Olenych, S.; Bonifacino, J. S.; Davidson, M. W.; Lippincott-Schwartz, J.; Hess, H. F. *Science* **2006,** 313, (5793), 1642-1645.
17. Hell, S. W.; Wichmann, J. *Opt. Lett.* **1994,** 19, (11), 780-782.
18. Hess, S. T.; Girirajan, T. P.; Mason, M. D. *Biophys. J.* **2006,** 91, (11), 4258-4272.
19. Rust, M. J.; Bates, M.; Zhuang, X. *Nat. Methods* **2006,** 3, (10), 793-796.
20. Rogers, E. T. F.; Lindberg, J.; Roy, T.; Savo, S.; Chad, J. E.; Dennis, M. R.; Zheludev, N. I. *Nat. Mater.* **2012,** 11, 432-435.
21. Yuan, G. H.; Zheludev, N. I. *Science* **2019,** 364, (6442), 771-775.
22. Pu, T.; Ou, J. Y.; Savinov, V.; Yuan, G.; Papasimakis, N.; Zheludev, N. I. *Adv. Sci.* **2020**, 2002886.
23. Zewail, A. H. *Science* **2010,** 328, (5975), 187-193.
24. Kwon, O.-H.; Barwick, B.; Park, H. S.; Baskin, J. S.; Zewail, A. H. *Nano Lett.* **2008,** 8, (11), 3557-3562.
25. Barg, A.; Tsaturyan, Y.; Belhage, E.; Nielsen, W. H. P.; Møller, C. B.; Schliesser, A. *Appl. Phys. B* **2017,** 123, 8.
26. Rothberg, S. J.; Allenb, M. S.; Castellinic, P.; Di Maiod, D.; Dirckxe, J. J. J.; Ewinsf, D. J.; Halkona, B. J.; Muyshondte, P.; Paonec, N.; Ryang, T.; Stegerh, H.; Tomasinic, E. P.; Vanlanduiti, S.; Vignolaj, J. F. *Opt. Laser Eng.* **2017,** 99, 11-22.
27. Buks, E.; Roukes, M. L. *Physical Review B* **2001,** 63, (3).
28. Nigues, A.; Siria, A.; Verlot, P. *Nat Commun* **2015,** 6, 8104.
29. Hauer, B. D.; Doolin, C.; Beach, K. S. D.; Davis, J. P. *Ann. Phys. - New York* **2013,** 339, 181-207.
30. Aspelmeyer, M.; Kippenberg, T. J.; Marquardt, F. *Rev. Mod. Phys.* **2014,** 86, (4), 1391-1452.
31. Unterreithmeier, Q. P.; Faust, T.; Kotthaus, J. P. *Phys. Rev. Lett.* **2010,** 105, (2), 027205.
32. Rieger, J.; Isacsson, A.; Seitner, M. J.; Kotthaus, J. P.; Weig, E. M. *Nat. Commun.* **2014,** 5, (1), 1-6.

33. Feynman, R. P. *Caltech Engineering and Science* **1960,** 23, 22-36.
34. Zheludev, N. I.; Plum, E. *Nature nanotechnology* **2016,** 11, (1), 16.
35. Ou, J. Y.; Plum, E.; Zhang, J.; Zheludev, N. I. *Adv Mater* **2016,** 28, (4), 729-33.

TABLE OF CONTENTS IMAGE